Journal of Solid State Chemistry 182 (2009) 1312–1318

Contents lists available at ScienceDirect

Journal of Solid State Chemistry

journal homepage: www.elsevier.com/locate/jssc

Structure and crystal chemistry of fluorite-related $Bi_{38}Mo_7O_{78}$ from single crystal X-ray diffraction and *ab initio* calculations

Neeraj Sharma [a,*], René B. Macquart [a,b], Mogens Christensen [b], Maxim Avdeev [b], Yu-Sheng Chen [c], Chris D. Ling [a,b]

[a] School of Chemistry, The University of Sydney, Sydney, NSW 2006, Australia
[b] Bragg Institute, Australian Nuclear Science and Technology Organisation, PMB 1, Menai, NSW 2234, Australia
[c] ChemMatCars, Advanced Photon Source, Argonne National Laboratories, Argonne, IL 60439, USA

ARTICLE INFO

Article history:
Received 22 November 2008
Received in revised form
11 February 2009
Accepted 27 February 2009
Available online 6 March 2009

Keywords:
Oxide ion conduction
Bismuth molybdenum oxide
Delta-Bi_2O_3
Single crystal X-ray diffraction
Synchrotron
Floating zone furnace

ABSTRACT

The floating-zone furnace method was used to synthesize single crystals of the fluorite-related δ-Bi_2O_3-type phase $Bi_{38}Mo_7O_{78}$ for the first time. Single crystal synchrotron X-ray diffraction data, in conjunction with *ab initio* (density functional theory) calculations, were used to solve, optimize, and refine the $5\times3\times3$ commensurate superstructure of fluorite-type δ-Bi_2O_3 in *Pbcn* ($a=28.7058(11)$ Å, $b=16.8493(7)$ Å and $c=16.9376(6)$ Å, $Z=4$, $R_F=11.26\%$, $wR_I=21.67\%$). The structure contains stepped channels of Mo^{6+} in tetrahedral environments along the *b* axis and chains of Mo^{6+} in octahedral environments along the *ac* plane. The role of the stepped channels in oxide ion conduction is discussed. The simultaneous presence of both tetrahedral and octahedral coordination environments for Mo^{6+}, something not previously observed in Mo^{6+}-doped δ-Bi_2O_3-type phases, is supported by charge balance considerations in addition to the results of crystallographic and *ab initio* analysis.

1. Introduction

Compounds representing stabilized versions of the high temperature form of bismuth oxide, δ-Bi_2O_3, generally feature high oxide ion conductivities [1,2]. The parent δ-Bi_2O_3 phase has a fluorite-type structure ($Fm\bar{3}m$ symmetry) with an average oxygen occupancy of 75% [3]. The conductivity is proposed to be due to the high concentration of oxide ion vacancies and the high polarizability of the cation network due to the stereochemically active $6s^2$ lone pair on Bi^{3+} ions [4]. In order to stabilize the δ-Bi_2O_3 structure to room temperature, transition metals dopant cations such as Nb^{5+}, Ta^{5+}, Cr^{6+}, Mo^{6+}, W^{6+}, and Re^{7+} [5–8] can be used. These often produce complex modulated structures at room temperature, with δ-Bi_2O_3-related substructures, while often retaining oxide ion conductivities at elevated temperatures similar to δ-Bi_2O_3 [2].

Bismuth-rich phases in the pseudo-binary Bi_2O_3–Mo_2O_6 system have been investigated for their oxide ion conductivities [1,4,9–11] and catalytic properties [12,13] in addition to their complex structures and crystal chemistry. Vannier et al. [9] described three types of oxide ion conductors in the molybdenum doped δ-Bi_2O_3-related structures; monodimensional, two- and three-dimensional. They reported the first observation of the monodimensional type in $Bi_{26}Mo_{10}O_{69-\delta}$. Two-dimensional conduction is found in layered structures such as $n=1$ Aurivillius phase *L*-Bi_2MoO_6 [14–16] and the related BIMEVOX [17] compounds, where oxide ions can move along planes. Three-dimensional conduction occurs in other δ-Bi_2O_3-related phases where oxide ions can move through the lattice without directional constraints.

This study concerns $Bi_{38}Mo_7O_{78}$, which was first reported by Buttrey et al. [18] who described it as a $3\times5\times3$ commensurate superstructure of fluorite-type δ-Bi_2O_3 in orthorhombic *Pccn*, on the basis of selected area electron diffraction. This supercell comprises 180 cations of which 152 are Bi and 28 are Mo. Later electron diffraction work supported this result and proposed several possible ordered models for the Bi/Mo cation array [5,19].

$Bi_{38}Mo_7O_{78}$ is a line-phase found between the reported 3-dimensionally incommensurate modulated phase $Bi_{42}Mo_8O_{87}$ [20] and the partially ordered superstructure phase $Bi_{14}MoO_{24}$ [21–24] in the Bi_2O_3–Mo_2O_6 phase diagram [25,26] (Fig. 1). The local Mo environment in $Bi_{14}MoO_{24}$ is tetrahedral. The structure of the incommensurately modulated phase has not been fully solved, but the coordination environment of Mo is thought to be tetrahedral in this case, analogous to the model proposed for $Bi_{1-x}Cr_xO_{1.5+1.5x}$ where $0.05\leqslant x\leqslant0.15$ [27]. A number of other phases with tetrahedrally coordinated Mo have been reported in this system, containing unique $[Bi_{12}O_{14}]_\infty$

* Corresponding author. Fax: +61 2 9351 3329.
E-mail address: n.sharma@chem.usyd.edu.au (N. Sharma).

0022-4596/$ - see front matter Crown Copyright © 2009 Published by Elsevier Inc. All rights reserved.
doi:10.1016/j.jssc.2009.02.030

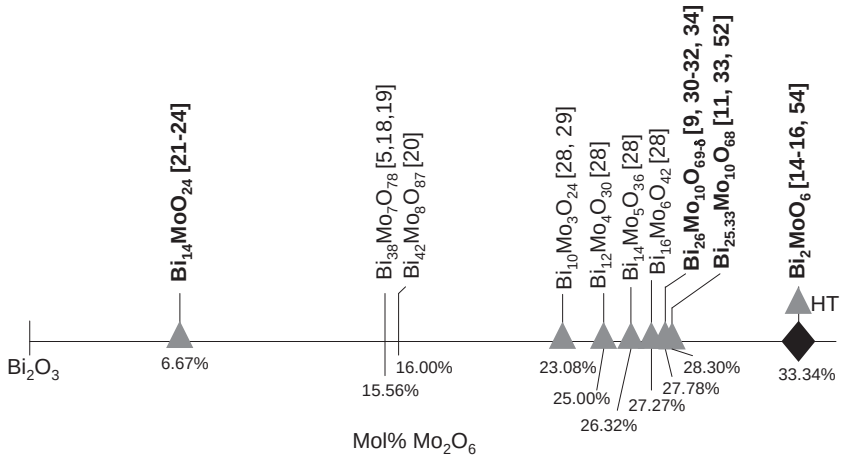

Fig. 1. Partial phase diagram of the pseudo-binary Bi_2O_3–Mo_2O_6 system showing tetrahedrally coordinated Mo phases with gray triangles and octahedrally coordinated Mo phases with black diamonds. High-temperature phases are labeled "HT". Full crystallographic refinements have been reported for the compounds in bold font. (E.g. Ref. [54]).

columns—$Bi_{2n+4}Mo_nO_{6(n+1)}$ $n=3$, 4, 5, 6, $Bi_{25.33}Mo_{10}O_{68}$ and $Bi_{26}Mo_{10}O_{69-\delta}$ [9,11,28–36]—at more Mo-rich compositions. The phase with the closest composition to $Bi_{38}Mo_7O_{78}$ containing octahedrally coordinated Mo is the $n=1$ Aurivillius phase L-Bi_2MoO_6 [14,15].

Recently, geometry optimizations of various commensurate superstructures of transition metal doped δ-Bi_2O_3 have been undertaken with *ab initio* calculations using density functional theory (DFT) [24,37]. In order to minimize computation time, the input model for geometry optimizations is based on the available information about the compound such as space-group symmetry, cell parameters, relationship to the parent δ-Bi_2O_3 subcell and cation distribution often collated from a number of sources. Depending on the size and complexity of the system being investigated, the general approach is to introduce oxygen atoms at the ideal fluorite-type positions in the superstructure. Oxygen vacancies are then introduced around the dopant cations, decreasing their coordination number from 8-fold to 6- or 4-fold as appropriate, based on crystal-chemical and charge-balance considerations. This provides the input model for DFT geometry optimization calculations. The largest distortions are expected at the oxygen sites around dopant cations. Finally, the DFT-optimized model is refined against neutron or X-ray diffraction data. If the final refinement produces only minor atomic shifts from the DFT-optimized positions, then the structural model is supported by two entirely independent methods, greatly increasing confidence in its veracity.

Here, we report the growth of single crystals of $Bi_{38}Mo_7O_{78}$ and their structural characterization using single-crystal synchrotron X-ray diffraction in conjunction with *ab initio* geometry optimization calculations. We compare the structure to those of other Mo-doped δ-Bi_2O_3-related phases and discuss potential oxide ion conduction pathways.

Table 1
Crystal and refinement details.

Composition	$Bi_{38}Mo_7O_{78}$	$Bi_{38}Mo_7O_{78}$
Crystal symmetry	Orthorhombic	Orthorhombic
Space group	*Pbcn*	*Pbcn*
a (Å)	28.7058(11)	28.5213(57)
b (Å)	16.8493(7)	16.7486(33)
c (Å)	16.9376(6)	16.8172(34)
Z	4	4
Volume (Å^3)	8192.3(5)	8033(3)
Density (g cm^{-3})	7.99	8.15
Data collection		
Source	Synchrotron	Synchrotron
Wavelength (Å)	0.41328	0.49694
Temperature (K)	293	100
Crystal size (μm^3)	~125	~125
Crystal color/shape	Transparent prism	Transparent prism
$h\,k\,l$ range	$-27\leqslant h\leqslant 49$, $-24\leqslant k\leqslant 29$, $-19\leqslant l\leqslant 28$	$0\leqslant h\leqslant 40$, $0\leqslant k\leqslant 23$, $0\leqslant l\leqslant 24$
Maximum 2θ	42.98	34.58
Number of measured reflections	143 301	166 569
Number of unique reflections	21 932	11 920
Number of reflections $I>\sigma(I)$	15 060	10 015
Merging R factor (%)	6.71	5.30
Refinement		
Number of refined parameters	332	332
R_F with $F_0/\sigma F_0>4$ (%)	7.39	6.75
R_F (%)	11.26	8.20
wR_I (%)	21.67	19.97
χ^2	0.988	1.057

2. Experimental

A stoichiometric mixture of Bi_2O_3 (Sigma Aldrich 5N) and MoO_3 (TJTM 3N6) was ground in a planetary ball mill (Retsch PM100) for 90 h at 350 rpm with breaks in rotation every 10 min for 10 s followed by grinding in the reverse direction. A small amount of ethanol was added to facilitate homogenous grinding. The sample was then heated at 750 °C for 3 h in an alumina crucible. Following heat treatment, the sample was pressed into rods at 60 MPa in a hydrostatic press. These rods were sintered at 750 °C for 1 h in a vertical tube furnace then mounted in an optical floating zone furnace (Crystal Systems Corporation FZ-T-10000-H-VI-VPM-PC) with 300 W filaments. The rods melted between 32% and 35% power and were taken through the hot zone at rates of 1–10 mm h^{-1} while rotating at 10–30 rpm.

The Bi:Mo ratio of the grown rod was confirmed using energy dispersive X-ray spectroscopy (EDS) in a Philips XL30 scanning electron microscope (SEM). Crystals were initially analyzed on a Bruker-Nonius APEX-II laboratory X-ray diffractometer with Mo $K\alpha$ radiation ($\lambda=0.71073$ Å). The 5 mm diameter synthesized rod was found to be polycrystalline, but to contain single crystals of up to $\sim 1\times 10^6$ μm^3. A small ($\sim$125 μm^3) crystal was selected for synchrotron X-ray diffraction on beamline ID-15-C at the

Advanced Photon Source, Argonne National Laboratories. Data were collected at 100 K at $\lambda = 0.49694$ Å on a Bruker 6000 CCD detector, and at room temperature (298 K) at $\lambda = 0.41328$ Å on a Bruker APEX-II detector. Data were integrated with SAINTPlus [38] and a SADABS [39] absorption correction was applied (Table 1). Structural refinements were carried out with the SHELX97 package [40] on the WinGX [41] front end.

First-principles calculations were carried out using DFT. Calculations used the projector-augmented wave (PAW) method [42,43], as implemented in the Vienna *ab initio* simulation package (VASP) [44,45], with the Perdew–Burke–Ernzerhof (PBE) [46] form of the generalized gradient approximation (GGA). Both atomic positions and unit-cell volume and shape were optimized with no symmetry constraints using a plane-wave energy cut-off 400 eV. Due to the large size of the unit cell (492 atoms) the calculations were performed only at the Γ point in reciprocal space. The Bi, Mo, and O atoms were treated in $6s^2 6p^3$, $4d^5 5s^1$, and $2s^2 2p^4$ valence states, respectively, using the standard VASP PAW potentials.

3. Results

Laboratory and synchrotron single crystal X-ray diffraction data were initially integrated on the basis of the reported orthorhombic *Pccn* space-group, since the Bi:Mo ratio from EDS was found to be 5.5(2):1 [5,18,19]. However, the systematic extinctions found via the program XPREP [47] determined that the true space-group was unambiguously *Pbcn*. The incorrect assignment of *Pccn* suggests that earlier electron diffraction studies failed to observe diffraction patterns along the unique [010] direction. Direct methods (SHELXS-97 [40]) were used to find the initial metal atom positions in the fluorite-type. All metals were initially defined as Bi. The occupancies were then refined, and those for which occupancies fell to approximately 1/2 were redefined as Mo, resulting in the expected stoichiometric ratio of Bi:Mo = 38:7.

The first set of oxygen atom positions, which were easily located in Fourier difference maps, consisted of fluorite-type sites with only Bi atoms as nearest neighbors. Subsequent oxygen atoms (those with Mo atoms as nearest neighbors) were much more difficult to locate in the Fourier difference maps, and once included in the model they could only be refined by placing constraints on Mo–O bond lengths and using isotropic atomic displacement parameters (ADPs). The model eventually obtained contained two crystallographic Mo sites with tetrahedral coordination (Mo1 and Mo2), and the remaining two with octahedral coordination (Mo3 and Mo4). The positions of the oxygen atoms forming tetrahedral environments could eventually be refined freely, but the positions of those forming octahedral environments had to be constrained.

The model thus obtained, with the expected stoichiometry $Bi_{38}Mo_7O_{78}$, was then tested and optimized using DFT calculations after relaxing the symmetry to *P*1. The optimized structure showed a maximum deviation of 0.035 Å from $P2_1/c$ space-group symmetry and of 0.20 Å from *Pbcn*. The optimization preserved both the octahedral and the tetrahedral coordination environments around Mo sites.

The DFT-optimized model was finally re-refined against single crystal synchrotron X-ray diffraction data. Positions and independent anisotropic ADPs were refined for metal atoms, followed by positions and independent isotropic ADPs for the fluorite-type oxygen atoms with exclusively Bi atoms as nearest neighbors. Oxygen atoms forming tetrahedral environments about Mo atoms then had their positions and independent isotropic ADPs refined. Finally, oxygen atoms forming octahedral environments about Mo atoms had a global isotropic ADP refined for each octahedron, while remaining fixed at their positions determined by DFT. Refinement details are presented in Table 1. Final refined atomic

Table 2
Final refined fractional atomic coordinates, ADPs, and bond valence sums (BVS) for $Bi_{38}Mo_7O_{78}$ at room temperature.

Atom	Wyckoff position	*x*	*y*	*z*	U_{eq}/U_{iso}	BVS
Bi1	8*d*	0.09962(2)	0.41767(4)	0.60267(4)	0.0161(1)	2.71
Bi2	8*d*	0.10452(2)	0.56791(4)	0.76073(4)	0.0201(1)	3.33
Bi3	8*d*	0.19455(3)	0.40073(5)	0.75009(5)	0.0274(1)	3.06
Bi4	8*d*	0.00440(3)	0.25349(5)	0.90660(7)	0.0374(2)	2.95
Bi5	8*d*	0.20180(2)	0.24530(4)	0.60097(4)	0.0177(1)	3.82
Bi6	8*d*	0.20351(2)	0.25425(4)	0.26443(4)	0.0172(1)	3.51
Bi7	8*d*	0.19953(2)	0.91555(4)	0.91663(4)	0.0187(1)	3.81
Bi8	8*d*	0.09831(2)	0.92821(4)	0.75441(4)	0.0183(1)	3.49
Bi9	8*d*	0.09489(5)	0.75665(6)	0.24008(7)	0.0551(3)	2.55
Bi10	8*d*	0.09269(2)	0.75707(4)	0.57066(4)	0.0179(1)	3.59
Bi11	8*d*	0.99772(2)	0.91914(5)	0.58705(4)	0.0227(1)	2.83
Bi12	8*d*	0.19369(2)	0.24134(4)	0.90127(4)	0.0173(1)	3.17
Bi13	8*d*	0.09995(2)	0.07775(4)	0.59975(4)	0.0198(1)	3.46
Bi14	8*d*	0.99956(2)	0.57256(4)	0.57956(4)	0.0166(1)	2.74
Bi15	8*d*	0.09789(2)	0.90207(5)	0.41752(4)	0.0220(1)	3.06
Bi16	8*d*	0.09065(2)	0.41188(4)	0.91598(4)	0.0172(1)	3.20
Bi17	8*d*	0.29658(2)	0.08104(4)	0.91936(4)	0.0143(1)	3.62
Bi18	8*d*	0.19638(2)	0.06742(5)	0.76020(5)	0.0277(1)	3.12
Bi19	4*c*	0	0.08006(11)	0.75	0.0437(3)	2.41
Bi20	4*c*	0	0.42176(8)	0.75	0.0297(2)	1.89
Mo1	8*d*	0.19419(5)	0.59396(1)	0.58006(9)	0.0214(2)	7.77
Mo2	8*d*	0.19680(5)	0.91101(12)	0.58659(9)	0.0241(3)	6.33
Mo3	8*d*	0.10206(5)	0.25303(9)	0.42743(9)	0.0190(2)	5.78
Mo4	4*c*	0	0.25405(16)	0.25	0.0575(12)	5.33
O1	8*d*	0.0416(5)	0.4831(8)	0.9818(8)	0.019(2)	2.43
O2	8*d*	0.1269(5)	0.4582(9)	0.7126(9)	0.021(2)	2.63
O3	8*d*	0.0559(5)	0.5059(9)	0.8301(9)	0.022(2)	2.26
O4	8*d*	0.1578(5)	0.3263(9)	0.8301(9)	0.022(3)	2.26
O5	8*d*	0.2361(6)	0.3393(10)	0.3390(9)	0.027(3)	2.32
O6	8*d*	0.0475(5)	0.9830(9)	0.6508(9)	0.026(3)	2.20
O7	8*d*	0.1587(5)	0.1459(9)	0.8348(9)	0.023(3)	2.37
O8	8*d*	0.0566(5)	0.1525(9)	0.6660(9)	0.023(3)	2.30
O9	8*d*	0.1591(5)	0.9704(9)	0.8280(9)	0.022(2)	2.38
O10	8*d*	0.0454(5)	0.3431(9)	0.8441(9)	0.025(3)	2.37
O11	8*d*	0.0551(5)	0.9984(10)	0.8253(9)	0.025(3)	2.10
O12	8*d*	0.1609(6)	0.3356(10)	0.6495(10)	0.031(3)	2.40
O13	8*d*	0.0540(6)	0.8319(10)	0.3463(9)	0.027(3)	2.27
O14	8*d*	0.0539(6)	0.6787(10)	0.4991(10)	0.031(3)	2.24
O15	8*d*	0.2314(6)	0.8343(11)	0.8406(11)	0.034(4)	2.31
O16	8*d*	0.0581(6)	0.3313(10)	0.6624(10)	0.029(3)	2.21
O17	8*d*	0.1303(6)	0.7868(11)	0.4673(11)	0.034(4)	2.43
O18	8*d*	0.0514(6)	0.8496(11)	0.5185(11)	0.034(4)	2.27
O19	8*d*	0.1320(6)	0.0269(11)	0.6986(11)	0.034(4)	2.74
O20	8*d*	0.2460(7)	0.0015(12)	0.8768(13)	0.042(4)	2.35
O21	8*d*	0.3416(8)	0.0234(13)	0.8414(13)	0.047(5)	2.17
O22	8*d*	0.2659(8)	0.2338(16)	0.2109(16)	0.060(6)	2.54
O23	8*d*	0.1557(12)	0.1655(19)	0.6500(19)	0.081(9)	2.12
O24	8*d*	0.2258(23)	0.6281(39)	0.5105(39)	0.196(26)	2.56
O25	8*d*	0.2105(15)	0.6153(27)	0.6722(27)	0.126(15)	2.13
O26	8*d*	0.1864(18)	0.4988(35)	0.5603(34)	0.162(19)	2.22
O27	8*d*	0.1358(16)	0.6215(29)	0.5755(29)	0.135(16)	1.87
O28	8*d*	0.1600(10)	0.8472(16)	0.6458(16)	0.063(7)	1.77
O29	8*d*	0.2324(9)	0.8506(15)	0.5268(15)	0.054(6)	1.94
O30	8*d*	0.2317(10)	0.9615(18)	0.6516(18)	0.071(8)	2.02
O31	8*d*	0.1648(9)	0.9703(16)	0.5257(16)	0.060(6)	2.14
O32	8*d*	0.1245[a]	0.3432[a]	0.3757[a]	0.356(26)[b]	1.71
O33	8*d*	0.0501[a]	0.3347[a]	0.4905[a]	0.356(26)[b]	1.24
O34	8*d*	0.1334[a]	0.1773[a]	0.3751[a]	0.356(26)[b]	1.83
O35	8*d*	0.0570[a]	0.1785[a]	0.4825[a]	0.356(26)[b]	1.37
O36	8*d*	0.1360[a]	0.2711[a]	0.5146[a]	0.356(26)[b]	1.86
O37	8*d*	0.0492[a]	0.2536[a]	0.3349[a]	0.559(71)[c]	1.40
O38	8*d*	0.5370[a]	0.8329[a]	0.3062[a]	0.559(71)[c]	1.41
O39	8*d*	0.5310[a]	0.6704[a]	0.3145[a]	0.559(71)[c]	1.57

Equivalent isotropic ADPs are given for metal atoms. Full details, including bond lengths and angles, are available in the deposited crystallographic information file (CIF).

[a] Positions fixed from the results of *ab initio* density functional theory calculations.

[b,c] Atomic displacements constrained to be equal.

positions, ADPs, and calculated bond valence sums (BVS) [48] are given in Table 2, selected bond lengths in Table 3 and the structural model is shown in Fig. 2.

4. Discussion

Clearly, previous difficulties encountered trying to solve the structure of $Bi_{38}Mo_7O_{78}$ were at least partly due to the incorrect assignment of the space-group as *Pccn*, rather than *Pbcn* [5,18,19]. However, the presence of Mo^{6+} cations in both octahedral and tetrahedral coordination environments is another unexpected feature that made structure solution more difficult and less intuitive. On a pseudo-binary phase diagram between Bi_2O_3 and Mo_2O_6 (Fig. 1), the known phases either side of $Bi_{38}Mo_7O_{78}$ feature Mo exclusively in tetrahedral coordination environments. Nevertheless, the model presented here is fully consistent with space group symmetry, the existence of Mo in the 6+ oxidation state expected for such a compound synthesized in air (no additional oxygen vacancies are required to satisfy stoichiometry), BVS calculations (see Table 2), and the DFT geometry optimizations that show it represents at least a local thermodynamic minimum.

The DFT-optimized structure has a smaller deviation from the monoclinic $P2_1/c$ space-group than it does from the orthorhombic *Pbcn* space-group, suggesting a possible low-temperature phase for this compound. The DFT calculations require a charge balanced cell without multiple occupancies and are effectively undertaken at 0 K. It is worth noting in this context that a previous single crystal synchrotron X-ray diffraction study of this compound [19] reported $\beta = 90.6^\circ$, although this was attributed to endemic twinning. In this study we saw no statistically significant deviation from *Pbcn* at either 298 or 100 K in our experimental data, and therefore transformed the DFT-optimized result to this space-group.

Buttrey et al. [18] saw evidence in high resolution transmission electron microscopy (HRTEM) of a diamond-like contrast in an ⟨110⟩-type fluorite projection, apparently due to cation ordering. The Mo atoms in our model also form diamond-like motifs along the *c* axis which corresponds to a ⟨110⟩-type fluorite projection, as seen in Fig. 2. No diamond-like motifs are seen in the other ⟨110⟩-type fluorite directions, also consistent with the HRTEM observations of Buttrey et al. [18] Note that the assignment of the cation array is further supported by the fact that ADPs for metal atoms in Table 1 all refine (freely) to reasonable values, generally ~0.02(1) Å^2. Mo4 has a slightly higher ADP (0.0575(12) Å^2) due to its location within the central octahedra of the octahedral chain, with Mo3 octahedra on either side.

The simultaneous presence of octahedral and tetrahedral coordination environments around a transition metal doped into

Table 3
Metal–oxygen bond lengths shorter than 3.3 Å in the refined structure of $Bi_{38}Mo_7O_{78}$.

Bond	Length (Å)	Bond	Length (Å)	Bond	Length (Å)	Bond	Length (Å)
Bi1–O1	3.12(1)	Bi7–O9	2.11(1)	Bi13–O6	2.36(1)	Bi19–O6	2.71(1)
Bi1–O2	2.13(1)	Bi7–O15	2.09(2)	Bi13–O8	2.10(1)	Bi19–O6	2.71(1)
Bi1–O12	2.37(2)	Bi7–O20	2.08(2)	Bi13–O19	2.10(2)	Bi19–O8	2.48(1)
Bi1–O16	2.14(2)	Bi7–O24	2.75(1)[a]	Bi13–O23	2.34(3)	Bi19–O8	2.48(1)
Bi1–O26	2.97(1)[a]	Bi7–O31	2.85(1)[a]	Bi13–O31	2.89(2)[a]	Bi19–O11	2.45(1)
Bi1–O33	2.75(1)[b]	Bi7–O34	2.56(1)[b]	Bi13–O35	2.89(2)[b]	Bi19–O11	2.45(1)
Bi1–O36	3.07(1)[b]	Bi8–O6	2.46(1)	Bi14–O1	2.18(1)	Bi19–O13	2.70(1)
Bi2–O2	2.12(1)	Bi8–O9	2.26(1)	Bi14–O1	2.25(1)	Bi19–O13	2.70(1)
Bi2–O3	2.10(1)	Bi8–O11	2.10(1)	Bi14–O3	2.47(1)	Bi20–O3	2.54(1)
Bi2–O21	2.20(2)	Bi8–O19	2.15(2)	Bi14–O14	2.73(1)	Bi20–O3	2.54(1)
Bi2–O32	2.52(1)[b]	Bi8–O28	2.91(1)[a]	Bi14–O33	2.43(1)[b]	Bi20–O10	2.45(1)
Bi2–O38	2.80(1)[b]	Bi8–O34	2.89(1)[b]	Bi14–O38	2.73(1)[b]	Bi20–O10	2.45(1)
Bi3–O2	2.26(1)	Bi8–O39	2.80(1)[b]	Bi15–O7	2.38(1)	Bi20–O16	2.71(1)
Bi3–O4	2.12(1)	Bi9–O4	2.74(1)	Bi15–O9	3.16(3)	Bi20–O16	2.71(1)
Bi3–O12	2.24(2)	Bi9–O7	2.93(2)	Bi15–O11	2.60(1)	Mo1–O24	1.60(6)[a]
Bi3–O15	2.84(1)	Bi9–O8	2.26(1)	Bi15–O13	2.11(1)	Mo1–O25	1.68(4)[a]
Bi3–O21	2.78(1)	Bi9–O10	2.82(1)	Bi15–O17	2.31(2)	Mo1–O26	1.65(6)[a]
Bi3–O22	2.61(2)	Bi9–O12	2.89(2)	Bi15–O18	2.35(2)	Mo1–O27	1.70(4)[a]
Bi3–O30	2.87(1)[a]	Bi9–O13	2.49(2)	Bi15–O31	2.89(1)[a]	Mo2–O28	1.80(3)[a]
Bi4–O8	2.73(1)	Bi9–O16	2.24(1)	Bi16–O1	2.16(1)	Mo2–O29	1.76(2)[a]
Bi4–O10	2.18(1)	Bi9–O23	2.67(3)	Bi16–O3	2.37(1)	Mo2–O30	1.70(3)[a]
Bi4–O13	2.27(2)	Bi10–O14	2.10(2)	Bi16–O4	2.81(2)	Mo2–O31	1.70(2)[a]
Bi4–O14	2.41(2)	Bi10–O17	2.12(2)	Bi16–O10	2.12(1)	Mo3–O32	1.87(1)[b]
Bi4–O16	2.50(2)	Bi10–O18	2.15(2)	Bi16–O14	2.33(2)	Mo3–O33	2.29(1)[b]
Bi4–O18	2.91(1)	Bi10–O27	2.62(5)[a]	Bi16–O21	2.99(1)	Mo3–O34	1.79(1)[b]
Bi4–O33	2.71(1)[b]	Bi10–O28	2.78(2)[a]	Bi16–O27	3.07(1)[a]	Mo3–O35	2.01(1)[b]
Bi4–O35	2.88(1)[b]	Bi10–O38	3.03(2)[b]	Bi17–O5	2.13(2)	Mo3–O36	1.80(1)[b]
Bi5–O12	2.09(2)	Bi10–O39	2.90(1)[b]	Bi17–O20	2.11(2)	Mo3–O37	2.18(1)[b]
Bi5–O22	2.11(3)	Bi11–O6	2.09(1)	Bi17–O21	2.09(2)	Mo4–O37	2.01(2)[b]
Bi5–O23	2.05(3)	Bi11–O11	2.50(1)	Bi17–O26	2.75(1)[a]	Mo4–O37	2.01(2)[b]
Bi5–O24	3.23(1)[a]	Bi11–O18	2.25(2)	Bi17–O29	2.83(1)[a]	Mo4–O38	1.95(2)[b]
Bi5–O29	2.89(1)[a]	Bi11–O35	2.58(1)[b]	Bi17–O32	2.70(1)[b]	Mo4–O38	1.95(2)[b]
Bi5–O36	2.42(1)[b]	Bi11–O39	2.44(1)[b]	Bi18–O5	2.83(2)	Mo4–O39	1.99(2)[b]
Bi6–O5	2.13(2)	Bi12–O4	2.14(1)	Bi18–O7	2.13(1)	Mo4–O39	1.99(2)[b]
Bi6–O15	2.14(2)	Bi12–O5	2.65(1)	Bi18–O9	2.27(1)		
Bi6–O22	2.03(2)	Bi12–O7	2.20(1)	Bi18–O19	2.23(2)		
Bi6–O25	2.69(4)[a]	Bi12–O15	2.85(1)	Bi18–O20	2.67(1)		
Bi6–O28	2.91(2)[a]	Bi12–O17	2.18(2)	Bi18–O23	2.75(3)		
Bi6–O34	3.04(1)[b]	Bi12–O24	3.04(1)[a]	Bi18–O25	3.18(1)[a]		
		Bi12–O29	2.86(1)[a]	Bi18–O30	2.78(3)[a]		

[a] Bonds where the O site is involved in a MoO_4 tetrahedron.
[b] Bonds where the O site is involved in a MoO_6 octahedron.

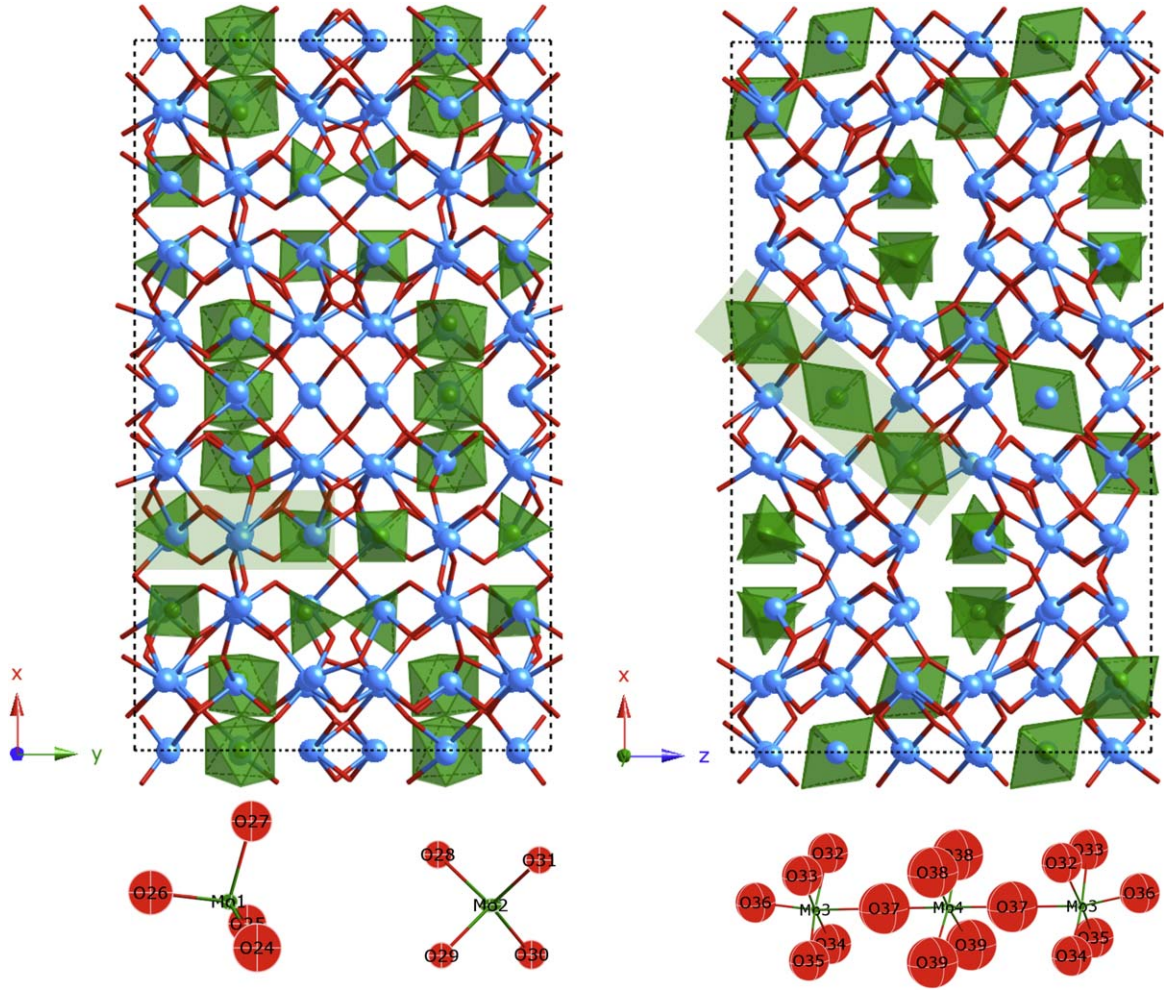

Fig. 2. The final refined structure of $Bi_{38}Mo_7O_{78}$ projected along the *z* (left) and *y* (right) directions, with MoO_4 tetrahedra and MoO_6 octahedra shown as green polygons, Bi atoms shown as blue spheres, and O atoms not bonded to Mo shown as red vertices on Bi–O bonds. Details of the Mo coordination environments are shown below as 50% probability thermal ellipsoid plots in the same projections (corresponding to the shaded parts of the complete drawings).

δ-Bi_2O_3 is not without precedent. X-ray powder diffraction (XRD), X-ray spectroscopy and infrared spectroscopy all indicate that 25% of the Re^{7+} sites in $Bi_{28}Re_2O_{49}$ are octahedrally coordinated and 75% tetrahedrally coordinated. [8] $Bi_2Al_4O_9$ [49,50] has equal amounts of tetrahedrally and octahedrally coordinated Al, with the octahedral units forming columns and the tetrahedral units in pairs, as in $Bi_{38}Mo_7O_{78}$. The structures of $Bi_2Al_4O_9$ and the related phase $Bi_2Fe_{4-x}Al_xO_9$ [51] were determined by XRD in conjunction with ^{27}Al solid state nuclear magnetic resonance (NMR) and ^{57}Fe Mössbauer spectroscopy, respectively. Unlike the $Bi_2M_4O_9$ series where *M* is a transition metal or semi-metal, $Bi_{38}Mo_7O_{78}$ features corner sharing MoO_6 octahedral units that do not extend throughout the structure but occur in groups along the *ac* plane. The MoO_4 tetrahedral units do extend in a stepped manner along the *b* axis; however, they are not connected. The discrepancy between $Bi_2M_4O_9$ and $Bi_{38}Mo_7O_{78}$ lies in the Bi:*M* ratio resulting in the formation of different structural types.

Much of the literature on $Bi_{26}Mo_{10}O_{69-\delta}$ [9,10,30–32,34] and its ordered form $Bi_{25.33}Mo_{10}O_{68}$ [11,33,52,53] has focused on oxide ion conduction, emphasizing: (a) the local disorder and rotational motion of nearest-neighbor MoO_4 tetrahedra in continuous channels and (b) the flexible coordination environment of Bi^{3+} with its stereochemically active $6s^2$ electron lone-pair. Some discussion of the coordination environments, bond lengths and BVSs around metal atoms in $Bi_{38}Mo_7O_{78}$ is therefore warranted here (Tables 2 and 3). Considering firstly the Mo sites, we note that the O atoms (O24–O31) tetrahedrally coordinated to Mo1 and Mo2 show slightly elevated ADPs in comparison with those bonded solely to Bi in fluorite-type positions. This is consistent with some rotational disorder of MoO_4 tetrahedra as observed for $Bi_{26}Mo_{10}O_{69-\delta}$ by NMR [10]. However, the O atoms (O32–O39) octahedrally coordinated to Mo3 and Mo4 have much larger ADPs that require some explanation. These O atoms were fixed at their DFT-optimized positions, which represent a local minimum, and the large refined ADPs are therefore strongly suggestive of long-range disorder. Free refinement of the positions of these atoms did not substantially improve the refinement statistics or reduce the ADPs, but led to slightly less regular octahedra, so the DFT-optimized positions were retained. The underbonding (according to BVS values) of all the O and Mo sites involved in MoO_6 octahedra shows that these Mo–O bonds are unusually long, which argues against the possibility that the true local coordination of Mo3 and Mo4 is tetrahedral as in $Bi_{14}MoO_{24}$ [21,23,24] (in which case the refined Mo–O bonds would be unusually short).

The bonding environments of Bi and O sites in the fluorite-type part of the structure are much more difficult to describe, due to the wide range of coordination numbers and geometries. A complete description for all 20 independent Bi atoms would be

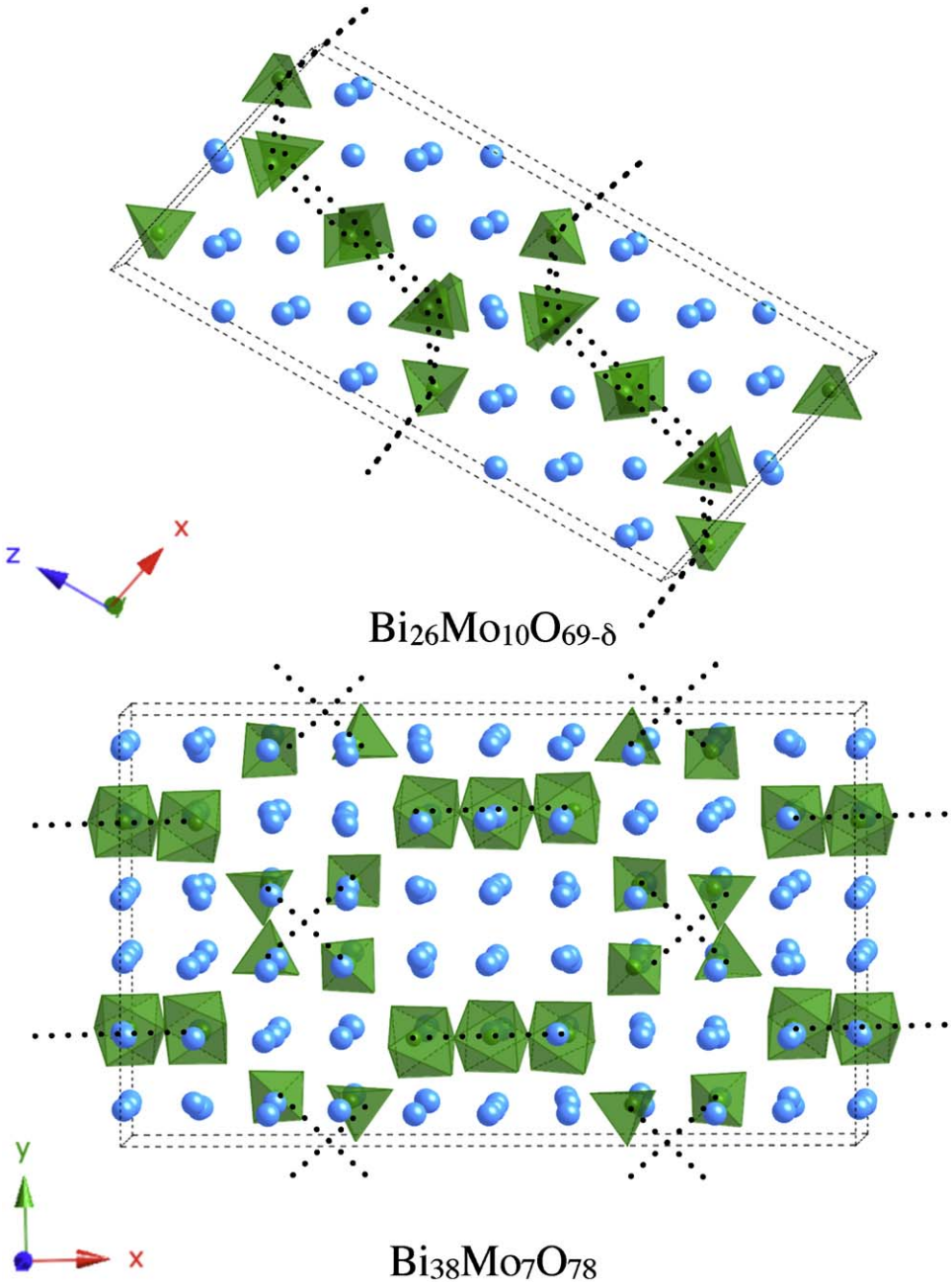

Fig. 3. Fluorite-like projections (close to $\langle 100 \rangle_F$) of $Bi_{26}Mo_{10}O_{69-\delta}$ [9] and $Bi_{38}Mo_7O_{78}$ highlighting the MoO_4 tetrahedra and MoO_6 octahedra by omitting oxygen atoms not bonded to Mo. Dotted lines connect Mo atoms that are "nearest neighbors" along $\langle 110 \rangle_F$ directions, the shortest paths between metal atoms.

unreasonably lengthy, so the essential details are summarized in Table 3 which includes all *M*–O bonds shorter than 3.3 Å. This cutoff captures all the cation–anion nearest neighbors of the fluorite-type parent structure, including those that have been highly distorted by the displacement of O atoms into MoO_4 tetrahedra and MoO_6 octahedra, and therefore indicates the effective coordination numbers of the various Bi sites, which vary from 5 to 8. It is interesting to compare this to the BVS values in Table 2 and note that the coordination numbers themselves are not responsible for extremes in BVS: the two 5-fold coordinate Bi sites (Bi2 and Bi11) are not significantly underbonded (BVS of 3.33 and 2.83); while the four 8-fold coordinate Bi sites (Bi4, Bi9, Bi18, and Bi19) are not significantly overbonded (BVS of 2.95, 2.55, 3.12 and 2.41). However, a clear correlation between BVS and coordination number is observed when the O sites in "pure" fluorite-type positions are differentiated from those involved in MoO_4 tetrahedra and MoO_6 octahedra (labeled [b] and [a], respectively, in Table 3). The Bi sites with BVS < 2.6 (Bi9, Bi19, Bi20) are the only ones that are not bonded to any Mo site, while the Bi sites with the highest BVS (Bi5, Bi6, Bi7, Bi10, Bi17) all have the most (two) independent coordinating O atoms involved in MoO_4 tetrahedra. This reflects the fact that Bi in ideal fluorite-type δ-Bi_2O_3 is rather underbonded, and the local distortions of O atoms due to transition metal dopants such as Mo help stabilize it.

Fig. 3 shows fluorite-like projections (close to $\langle 100 \rangle_F$) of $Bi_{26}Mo_{10}O_{69-\delta}$ and $Bi_{38}Mo_7O_{78}$ highlighting the MoO_4 tetrahedra and MoO_6 octahedra by omitting oxygen atoms not bonded to Mo. Dotted lines connect Mo atoms that are "nearest neighbors" along $\langle 110 \rangle_F$ directions, the shortest paths between metal atoms, and therefore represent the possible pathways for oxide ion

conduction when the Mo coordination environments become disordered at high temperatures. $Bi_{26}Mo_{10}O_{69-\delta}$ contains continuous channels of this type, and it has been shown that oxide ion conduction in this compound occurs along these channels via a partially occupied oxygen site in between the MoO_4 tetrahedra [9,11,52,53]. Recent work with ^{17}O NMR suggests that conduction is also facilitated by rapid and concerted rotational motions of the MoO_4 tetrahedra above 200 °C, while above 350 °C other motions involving the outermost oxygen atoms of the $[Bi_{12}O_{14}]_\infty$ columns and the MoO_4 tetrahedra begin to occur along the *ac* plane and *b* directions [10]. In contrast, $Bi_{38}Mo_7O_{78}$ only contains isolated Mo groups linked along $\langle 110 \rangle_F$ directions, consisting of two MoO_4 tetrahedra or three MoO_6 octahedra, leading to the expectation of less efficient oxide ion conductivity. However, this does not necessarily mean that the conductivity will be lower, because increasing transition metal content often leads to lower conductivity in transition metal-doped δ-Bi_2O_3-related structures [2]. Detailed measurements and comparisons of ionic conductivity, which are beyond the scope of this study, would shed further light on this question.

5. Conclusions

Cation ordering in $Bi_{38}Mo_7O_{78}$ has been unambiguously determined by single crystal synchrotron X-ray diffraction. The complete structure has been solved and refined using these data in conjunction with *ab initio* geometry optimization calculations. The space-group of $Bi_{38}Mo_7O_{78}$ is orthorhombic *Pbcn* as opposed to earlier reports of *Pccn*. This structure is unique in the pseudo-binary Bi_2O_3–Mo_2O_6 system as Mo atoms are present in both octahedral and tetrahedral oxygen coordination environments. The octahedrally coordinated Mo atoms form corner-connected groups in the *ac* plane, whilst the tetrahedrally coordinated Mo atoms form pairs in the *ab* plane. The larger displacement parameters on the oxygen atoms coordinating Mo sites may indicate some local disorder.

However, unlike $Bi_{26}Mo_{10}O_{69-\delta}$, $Bi_{38}Mo_7O_{78}$ does not contain continuous MoO_4 channels that could mediate oxide-ion conduction.

The initial structural solution derived from single crystal synchrotron X-ray diffraction was used as a starting model for *ab initio* (DFT) calculations. The DFT calculations provided further justification, which is independent in the geometry optimization routine, that the structural model is a minimum energy state. This three-step process (i.e. structural solution from diffraction → DFT geometry optimization calculations → re-refinement against diffraction data) again proves to be a very powerful method for understanding commensurately modulated structures based on δ-Bi_2O_3.

Acknowledgments

This work was supported by the Australian Research Council—Discovery Projects (DP0666465) and the Australian Institute of Nuclear Science and Engineering Postgraduate Research Awards scheme. Collection of synchrotron X-ray diffraction data at the Advanced Photon Source was supported by the Australian Synchrotron Research Program, which is funded by the Commonwealth of Australia under the Access to Major Research Facilities Program. Use of the Advanced Photon Source is supported by the US Department of Energy, Office of Science, Office of Basic Energy Sciences, under Contract no. DE-AC02-06CH11357.

References

[1] N.M. Sammes, G.A. Tompsett, H. Nafe, F. Aldinger, J. Eur. Ceram. Soc. 19 (1999) 1801–1826.
[2] T. Takahashi, H. Iwahara, Mater. Res. Bull. 13 (1978) 1447–1453.
[3] G. Gattow, H. Schröder, Z. Anorg. Allg. Chem. 318 (1962) 176–189.
[4] J.C. Boivin, G. Mairesse, Chem. Mater. 10 (1998) 2870–2888.
[5] C.D. Ling, R.L. Withers, S. Schmid, J.G. Thompson, J. Solid State Chem. 137 (1998) 42–61.
[6] Y.H. Liu, J.B. Li, J.K. Liang, J. Luo, L.N. Ji, J.Y. Zhang, G.H. Rao, Mater. Chem. Phys. 112 (2008) 239–243.
[7] A.K. Cheetham, A.R.R. Smith, Acta Cryst. B 41 (1985) 225–230.
[8] T.E. Crumpton, J.F.W. Mosselmans, C. Greaves, J. Mater. Chem. 15 (2005) 164–167.
[9] R.N. Vannier, F. Abraham, G. Nowogrocki, G. Mairesse, J. Solid State Chem. 142 (1999) 294–304.
[10] L. Holmes, L. Peng, I. Heinmaa, L.A. O'dell, M.E. Smith, R.N. Vannier, C.P. Grey, Chem. Mater. 20 (2008) 3638–3648.
[11] J. Galy, R. Enjalbert, P. Rozier, P. Millet, Solid State Sci. 5 (2003) 165–174.
[12] Ph.A. Batist, A.H.W.M. Der Kinderen, Y. Leeuwenburgh, F.A.M.G. Metz, G.C.A. Schuit, J. Catal. 12 (1968) 45–60.
[13] D.H. Galvan, S. Fuentes, M. Avalos-Borja, L. Cota-Araiza, J. Cruz-Reyes, E.A. Early, M.B. Maple, Catal. Lett. 18 (1993) 273–281.
[14] A.F. Van Den Elzen, G.D. Rieck, Acta Cryst. B 29 (1973) 2436–2438.
[15] F.R. Theobald, A. Laarif, A.W. Hewat, Ferroelectrics 56 (1984) 219–237.
[16] B. Aurivillius, Ark. Kemi. 5 (1952) 39–47.
[17] F. Abraham, J.C. Boivin, G. Mairesse, G. Nowogrocki, Solid State Ionics 40/41 (1990) 934–937.
[18] D.J. Buttrey, D.A. Jefferson, J.M. Thomas, Mater. Res. Bull. 21 (1986) 739–744.
[19] C.D. Ling, J. Solid State Chem. 148 (1999) 380–405.
[20] M. Valldor, S. Esmaeilzadeh, C. Pay-Gomez, J. Grins, J. Solid State Chem. 152 (2000) 573–576.
[21] C.D. Ling, R.L. Withers, J.G. Thompson, S. Schmid, Acta Cryst. B 55 (1999) 306–312.
[22] G. Spinolo, C. Tomasi, Powder Diffr. 12 (1997) 16–19.
[23] T.E. Crumpton, M.G. Francesconi, C. Greaves, J. Solid State Chem. 175 (2003) 197–206.
[24] C.D. Ling, Physica B 385–386 (2006) 193–195.
[25] M. Egashira, K. Matsuo, S. Kagawa, T. Seiyama, J. Catal. 58 (1970) 409–418.
[26] G. Bergerhoff, I.D. Brown, in: F.H. Allen, G. Bergerhoff, R. Sievers (Eds.), Crystallographic Databases, International Union of Crystallography, Chester, 1987, pp. 77–95.
[27] S. Esmaeilzadeh, S. Lundgren, U. Halenius, J. Grins, J. Solid State Chem. 156 (2001) 168–180.
[28] E. Vila, A.R. Landa-Canovas, J. Galy, J.E. Iglesias, A. Castro, J. Solid State Chem. 180 (2007) 661–669.
[29] E. Vila, J.E. Iglesias, J. Galy, A. Castro, Solid State Sci. 7 (2005) 1369–1376.
[30] D.J. Buttrey, T. Vogt, G.P.A. Yap, A.L. Rheingold, Mater. Res. Bull. 32 (1997) 947–963.
[31] R.N. Vannier, G. Mairesse, F. Abraham, G. Nowogrocki, J. Solid State Chem. 122 (1996) 394–406.
[32] M. Huve, R.N. Vannier, G. Mairesse, J. Solid State Chem. 149 (2000) 276–283.
[33] R. Enjalbert, G. Hasselmann, J. Galy, J. Solid State Chem. 131 (1997) 236–245.
[34] L.Y. Erman, E.L. Galperin, B.P. Soboler, Russ. J. Inorg. Chem. (Engl. Transl.) 16 (1971) 258.
[35] S. Miyazawa, A. Kawana, H. Koizumi, H. Iwasaki, Mater. Res. Bull. 9 (1974) 41–52.
[36] T. Chen, G.S. Smith, J. Solid State Chem. 13 (1975) 288–297.
[37] C.D. Ling, M. Johnson, J. Solid State Chem. 177 (2004) 1838–1846.
[38] SAINTPlus: v. 6.45, Data Reduction and Correction Program, Bruker AXS, 2001.
[39] SADABS Multi-Scan Absorption Correction Program, Bruker AXS, 2001.
[40] G.M. Sheldrick, SHELX97 Programs for Crystal Structure Analysis, University of Gottingen, 1997.
[41] L.J. Farrugia, J. Appl. Crystallogr. 32 (1999) 837–838.
[42] P.E. Blochl, Phys. Rev. B 50 (1994) 17953–17979.
[43] G. Kresse, D. Joubert, Phys. Rev. B 59 (1999) 1758–1775.
[44] G. Kresse, J. Furthmuller, Phys. Rev. B 54 (1996) 11169–11186.
[45] G. Kresse, J. Hafner, Phys. Rev. B 47 (1993) 558–561.
[46] J.P. Perdew, K. Burke, M. Ernzerhof, Phys. Rev. Lett. 77 (1996) 3865–3868.
[47] XPREP—Data preparation and reciprocal space exploration, Bruker AXS, 2001.
[48] N.E. Brese, M. O'keeffe, Acta Cryst. B 47 (1991) 192–197.
[49] I. Abrahams, A.J. Bush, G.E. Hawkes, T. Nunes, J. Solid State Chem. 147 (1999) 631–636.
[50] N. Niizeki, M. Wachi, Z. Kristallogr. 127 (1968) 173.
[51] D.M. Giaquinta, G.C. Papaefthymiou, H.-C. Zur Loye, J. Solid State Chem. 114 (1995) 199–205.
[52] B. Bastide, S. Villain, R. Enjalbert, J. Galy, Solid State Sci. 4 (2002) 599–608.
[53] J. Galy, P. Salles, P. Rozier, A. Castro, Solid State Ionics 177 (2006) 2897–2902.
[54] G. Blasse, J. Inorg. Nucl. Chem. 28 (1966) 1124–1125.